Silicon anodes for lithium-ion batteries produced from recovered kerf powders

Nils Peter Wagner[a,b,*], Artur Tron[a], Julian Richard Tolchard[a], Gianluigi Noia[c], Martin Pawel Bellmann[a]

[a] Department of Sustainable Energy Technology, SINTEF Industry, 7491 Trondheim, Norway

[b] Department of Materials Science and Engineering, Norwegian University of Science and Technology, 7491 Trondheim, Norway

[c] Garbo Srl, 28065 Cerano, Italy

* Corresponding author. Tel.: +47 45060739

E-mail address: nils.peter.wagner@sintef.no

Abstract

Silicon kerf waste from a photovoltaic silicon production process is assessed as an anode material for application as a lithium ion battery anode. In contrast to previous studies, the Si-kerf is used as-produced, with no chemical treatment or physical processing beyond solvent PEG removal. The as-produced Si-kerf performed as well as, or better than, previously reported Si-kerf anodes and is found to outperform a cleaned Si-kerf sample from blade sawing with a larger particle size. This highlights the advantage of the diamond wire cutting process, which yields relatively small particles. In half-cell testing, a cycle life >300 cycles at a capacity of 1000 $mAhg^{-1}$ is achieved with high levels of FEC addition. Full-cell testing against an NMC 442 cathode resulted in specific capacities up to 150 mAh g^{-1} (NMC), with the Si-kerf a relatively high degree of lithium consumption arising from repeated SEI formation and repair. It is concluded that pure Si-kerf is unsuitable for commercial application in Li-ion cells.

Keywords: Silicon anode; Kerf powder; Lithium ion battery; NMC Si Full-cell; Waste recycling; High capacity

1. Introduction

Lithium-ion batteries outperform all other commercial battery technologies due to their high gravimetric and volumetric energy density, power rate capability and long calendar lifetime [1-2], and consequently enjoy widespread adoption across all areas of energy storage. For high capacity applications, especially

in the electric transport sector, there is a need to further increase their energy density, which necessitates the development of new electrode materials with higher specific capacity. Although current generation cathode materials are the most limiting factor in this respect, showing specific capacities in the range 120-200 mAh g^{-1}, most efforts in improving energy density are concentrated on anode material development [3-4]. This is because there is no obviously better cathode chemistry to develop and optimise, but several promising anode candidates. Graphite is the commonly used anode material and displays a maximum specific capacity of 372 mAh g^{-1}. A number of alloy and conversion materials are reported to exhibit capacities well in excess of 1000 mAh g^{-1}, sufficient to have a profound effect on the overall capacity of a LiB, even with state-of-the-art positive electrode materials. Silicon (Si) is perhaps the most attractive and promising next generation anode material due to the high theoretical specific capacity of the formed $Li_{15}Si_4$ (3579 mAh g^{-1}) or $Li_{22}Si_5$ (4200 mAh g^{-1}) alloys [5-6], and is already incorporated in small quantities (~5%) in commercial cells The lithiation of Si occurs at low potentials vs. Li/Li^+ resulting in a low operating voltage of the anode (0.4 V vs. Li/Li^+). Furthermore, Si is non-toxic and environmentally friendly, highly abundant and inexpensive due to its' widespread applications in electronics [7]. Although Si has significant capacity advantages compared to graphitic anode materials, the use of Si in commercial LIBs is limited due to the low cycling stability of bulk Si: The uptake of up to 4 Li atoms per Si atom during lithiation is accompanied by a volume change of over 300%. Such volume changes upon lithiation and delithiation result in the degradation of the silicon particle structure and the loss of contact between electrode and current collector. Liu et al. [8] defined a critical particle diameter of 150 nm under which the full lithiation of Si particles should not result in particle rupture, which is somewhat smaller than can be easily achieved via traditional powder processing technologies. A second issue is the continuous electrolyte consumption resulting from repeated solid electrolyte interphase (SEI) formation following the detachment of the SEI from the particle surface upon delithiation. Combined, these issues result in lowered coulombic efficiency and cycling stability and thus severe capacity fade upon cycling [9]. Several approaches to overcome these issues, and improve the performance of Si anodes, have been investigated, including the application of Si in various nanostructures and morphologies, the use of Si based composites, and the utilisation of 3D current collectors [10].

An estimated 180 000 tons of high purity Si is produced for the photovoltaic and semiconductor industry annually, approximately 45–55% of which is consumed during the sawing process and is classified as

waste "kerf" material. [11]. The sawing of Si ingots is generally performed using a steel wire saw. This may be used in conjunction with a SiC/polyethylene glycol (PEG) slurry that acts as a combined coolant and abrasive medium (wire/slurry sawing), or in the form of a diamond-encrusted steel wire in which the abrasive is attached to the wire, which is cooled using PEG (diamond wire sawing). Both processes yield a fine Si sawdust, of a particle size potentially suitable for use as Li-ion battery anodes. The diamond wire process gives a "cleaner" product however, with the Si sawdust being dispersed in PEG with limited metal contamination. The slurry process produces a blended Si SiC slurry, also with some metal contamination [12-15].

The use of Si-kerf particles in anodes for LiBs has previously been reported with different means of cleaning and post treatment [13-19]. Kim et al. reported a Si-kerf/graphene oxide blend with a high initial reversible capacity of about 1600 mAh g^{-1} and a capacity retention of approximately 65% after 50 cycles [14]. Another study reported the preparation of a Si-carbon composite based on silicon kerf with a pyrolyzed biomass-based carbon coating [17]. The authors demonstrated a capacity of 955 mAh g^{-1} with 83% capacity retention after 51 cycles at a current density of 300 mA g^{-1}. Kasukabe et al. showed 800 cycles at 1200 mAh g^{-1} for bead milled Si-kerf employing buffered sodium carboxymethyl cellulose (Na-CMC) as binder and the addition of 10% of fluoroethylene carbonate (FEC) and 2% of vinylene carbonate (VC) as SEI-forming additives [13]. It should be noted that the difficulty of post-processing the kerf is dependent on the sawing process, as the kerf sludge from the slurry process contains SiC abrasive which must be removed. As metal impurities can have an impact on the physicochemical and electrochemical performance, the kerf often undergoes an acid treatment. Zhang et al. reported stable cycling for 200 cycles with a high capacity of about 2700 mAh g^{-1} and minimal losses for a surface modified Si-kerf sample [19]. The reported material studied underwent a relatively complex pre-treatment: Cleaning with diluted hydrochloric acid to remove metal contaminations, removal of the native oxide layer with hydrofluoric acid and then treatment with a sulfuric acid hydrogen peroxide mixture to form an SiO_x surface layer. The authors showed that the surface modification after the cleaning procedure was crucial for cycling stability. It is noted that in all published literature, Si-kerf was extensively post processed before Li-ion cell testing, which will increase the price of this waste product tremendously. In this paper, we report the physiochemical and electrochemical properties of diamond wire Si-kerf from the Norwegian solar industry. In contrast to previous studies, the only post processing the Si-kerf underwent was an acetone washing to remove polyethylene glycol.

2. Experimental

2.1. Si-kerf treatment

The Si-kerf used as a basis for this study was delivered from NorSun AS (Norway), where it is a waste product from Si N type single crystal diamond wire cutting for PV applications. As glycol was used as a coolant during the cutting process, the Si-kerf was received in a glycol-based suspension. This suspension was washed with acetone to fully remove the glycol. As a comparative reference a second diamond wire cut Si-kerf was acquired from a second commercial silicon powder supplier. This differed in having undergone a proprietary chemical post-processing to enhance electrochemical performance.

2.2. Physicochemical characterisation

The Si-kerf was analysed by inductively coupled plasma (ICP) optical emission spectroscopy (Thermo Scientific iCAP 7000, series ICP-OES) to determine the degree of foreign element contamination. The carbon and oxygen content were determined by total combustion on LECO carbon and oxygen analysers (Models TC 136 and CS444 for oxygen and carbon respectively). The particle size distribution (PSD) was measured by laser diffraction on a Microtrac S3500 particle size analyser. Crystal structure analysis was performed using powder X-ray diffraction (XRD) using a Bruker D8 Advance DAVINCI working in Bragg−Brentano (Θ/2Θ) geometry and utilising Cu Kα radiation. Nitrogen adsorption was applied to determine the surface area and porosity of the Si-kerf using the Brunauer−Emmett−Teller (BET) theory, T-plot, and Barrett−Joyner−Halenda (BJH) theory, using a Micrometrics Tristar 3000. Prior to nitrogen absorption analysis, the powder was vacuum dried at 250°C for 24 h. As-received Si-kerf powder and processed electrodes were imaged using Hitachi S-3400N and S-5500 Scanning Electron Microscopes (SEM). For cross sectional imaging of processed electrodes samples were immersed in liquid nitrogen and broken to give an accurate representation of the structure. Prior to imaging, powder samples were coated with a thin layer of carbon to enhance conductivity. Electrode cross sections were imaged without coating.

2.3. Electrochemical characterisation

Electrodes were processed by tape casting an aqueous slurry on Cu foil. The solids component of the slurry consisted of Si-kerf, conductive carbon (Super C 65, Timcal), and sodium carboxymethyl cellulose (Na-CMC, Aldrich, average Mw ~90,000) in a ratio of 70:15:15. The Na-CMC was utilised in the form of a pH3 buffered solution. This buffer comprised a 250 mL solution incorporating 23.65 mmol citric acid and 9.25 mmol KOH, into which 5 wt% Na-CMC was dissolved in the buffer by vigorous stirring at 70°C for 2 h. As the buffer components do not evaporate during the drying process the corrected electrode ratio was 65.4:13.9:14.05:6.7 (Si:Super C:Na-CMC:Buffer). Buffering the Na-CMC binder at pH 3 has been shown to protonate the carboxy groups of CMC and hence facilitate esterification between the native oxide layer of the Si-kerf and the carboxy groups of CMC [20-21].

As-cast electrodes were dried at room temperature until visibly dry, then vacuum dried at 90°C for 12 h. The dry cast had a thickness of approximately 10 µm and a Si loading of 0.7 mg cm^{-2}. Circular electrodes with a diameter of 16 mm were punched and transferred to an Ar filled glove box with H_2O and O_2 levels of < 0.1 ppm. Electrochemical characterisation was performed in CR 2016 coin cells (Hohsen Corp.) using either a circular Li counter electrode or a $LiNi_{0.4}Mn_{0.4}Co_{0.2}O_2$ (NMC) cathode (BC-723K 3M) as counter electrode, a porous polypropylene separator (Celgard 2400) and 40 µL electrolyte. The electrolyte used consisted of 1 M $LiPF_6$ dissolved in a 1:1 volume ratio of ethylene carbonate/diethyl carbonate mixture (Aldrich Battery grade). Fluoroethylene carbonate was added to the electrolyte blend as SEI formation additive. Electrolytes with FEC additions of 0, 5, 10 and 15 vol.% were evaluated. Cells were tested on Maccor 4200 and LANHE CT2001A galvanostatic cyclers. Half-cell testing was initiated with a four-cycle formation procedure at C/20 (1 C = 3600 mA g^{-1} of Si) adapted from Philippe et. al. [22]. The Si electrode was lithiated to a capacity of 500, 1000, 1500 and 2000 mAh g^{-1} while the corresponding lithiation was cut-off at 1 V vs. Li/Li^+. After the formation, the cells were either cycled in a voltage window of 0.05-1 V vs. Li/Li^+, or with a lithiation limitation to 1000 mAh g^{-1} and a corresponding delithiation to 1 V vs. Li/Li^+. Long-term cycling was performed at C/5, whilst the rate performance was evaluated at different C-rates between C/20 and 1 C. The performance of the from diamond wire sawing was compared to a Si-kerf originating from blade cutting of Si ingots. The sample is from an undisclosed producer and underwent a purification procedure. The element distribution, XRD, SEM and particle size analysis of this Si-kerf can be found in the supplementary information. (Table S1, Figure S1-S2). The

electrodes were prepared in the same manner and had the same mass loading. For full-cell testing the Si electrode was balanced to approximately 1000 mAh g^{-1} of Si for a nominal NMC capacity of 160 mAh g^{-1}. The NMC cathodes were processed by slurry-based tape casting using conductive carbon (Super C 65, Imerys) and PVDF (Kynar) as binder in a mass ratio of 85:10:5. PVDF was dissolved in NMP prior to mixing and the solid to solvent ratio was approximately 1:2.5. NMC-Si Full-cells were cycled between 2.5 and 4.2 V. The electrode conditioning was performed for 2 cycles at low C-rate of C/10, where 1 C was defined as 160 mA g^{-1} (NMC). Long term cycling was performed at C/2, with CC-CV mode upon charge, where the potential was kept constant until the current dropped below C/10. The rate performance upon discharge was evaluated between C/10 and 2C, where the maximum charge current was set to C/2 including the aforementioned constant voltage step. Electrochemical post mortem analysis was performed to analyse the degradation of both electrodes separately. The full-cells were disassembled and reassembled into half-cells. To maintain the SEI and cathode interface the electrodes were not washed before reassembly.

3. Results and Discussion

3.1. Material characterisation

The metal contaminations, as determined by ICP-OES are shown in Table 1. The total concentration of foreign elements on the kerf surface after wafer sawing was 109.887 ppm, with Ni being the main contaminant at 97.429 ppm. The foreign metal contaminations arise from the sawing process and the impurities are believed to be present on the particle surface or as discrete particles. Metallic impurities should have a positive influence on the surface conductivity of the Si-kerf. The oxygen and carbon content of the diamond wire cut kerf sample were analysed by total combustion to be about 6.5 wt% and below 1 wt% respectively. The high oxygen value is due to the extremely large specific surface area and surface oxidation. The 6.5 wt.% oxygen value is in line with literature data suggesting an expected 10-20 Å of native oxide thickness [23].

Table 1. Metal contaminants by ICP-OES (values in ppm)

Element	Al	B	Ca	Cr	Cu	Fe	K	Li	Na

conc. (ppm)	0.204	<0.01	5.587	0.080	0.146	3.418	<0.01	<0.01	1.666
Element	**Ni**	**Pb**	**Zn**	**Mg**	**Mn**	**Ti**	**W**	**Co**	**Sb**
conc. (ppm)	97.429	<0.01	0.436	0.740	<0.01	0.181	<0.01	<0.01	<0.01

The N_2 adsorption/desorption isotherm, the particle size distribution according to laser diffraction and the powder XRD pattern of the Si-kerf are illustrated in Figure 1 a, b, c respectively. The isotherm resembles a type-II isotherm of a non-porous solid with a large flat region corresponding to the monolayer adsorption as shown in Figure 1a. The BET surface area was calculated to be 17.06 +- 0.12 m^2g^{-1}.

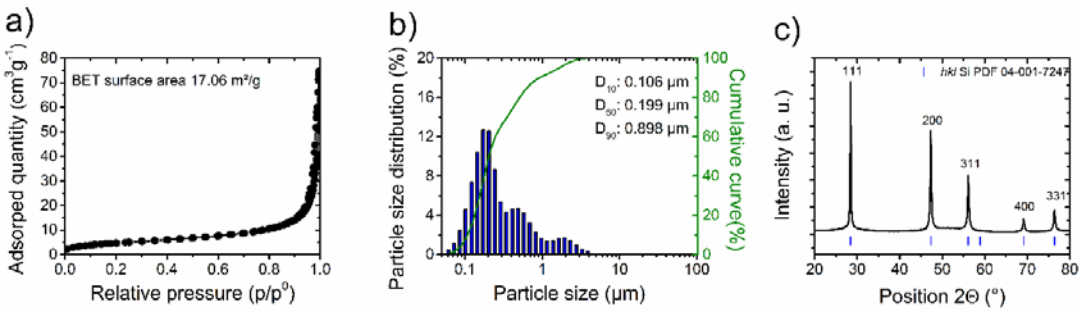

Figure 1. (a) N_2 adsorption and desorption isotherm of the diamond wire cut Si-kerf, (b) Particle size distribution of the Si-kerf including D values and the cumulative curve, (c) Powder XRD pattern of the diamond wire sawn Si, including database reference. Particle size distribution and XRD data for the blade-cut sample are presented in supplementary figures S1 and S2

The laser diffraction data (Figure 1b) indicates that the diamond wire sawn sample is mostly comprised of particles well below 1 µm in size. The particle size distribution is multimodal with a D_{50} value of 199 nm. Imaging of the sample with SEM (Figure 2) supports this, and suggests that the laser diffraction signal corresponding to larger particles in the range of 1-4 µm is probably due to agglomerates that were not broken up by ultrasonication prior to measurement. The Si-kerf is seen to consist of irregular shaped angular particles mostly in the sub-micron range. The irregularity of the particle size and the angular shape are not unexpected from the sawing of a brittle material such as silicon. The powder XRD pattern corresponds to that of crystalline Si (ICCD PDF-4+ 04-001-7247) as shown in Figure 1c. No additional phases were observed. The diffraction peaks were observed to exhibit a mild super-lorentzian peak

shape, suggestive of a broad crystallite size distribution extending down to the nanoscale. This is in good accord with the results seen from the particle size measurement and SEM imaging (Figure 2). In contrast, the blade-sawn sample exhibits more monomodal size distribution with a much larger D50 value of 4.3µm (Supplementary S2), and a tail extending down to around 100nm. The super-lorentzian peak shape evident in the XRD pattern of the diamond wire sawn sample is also absent (Supplementary S1). A similar angular particle morphology as for the diamond wire sawn sample is observed by SEM imaging (Supplementary S2).

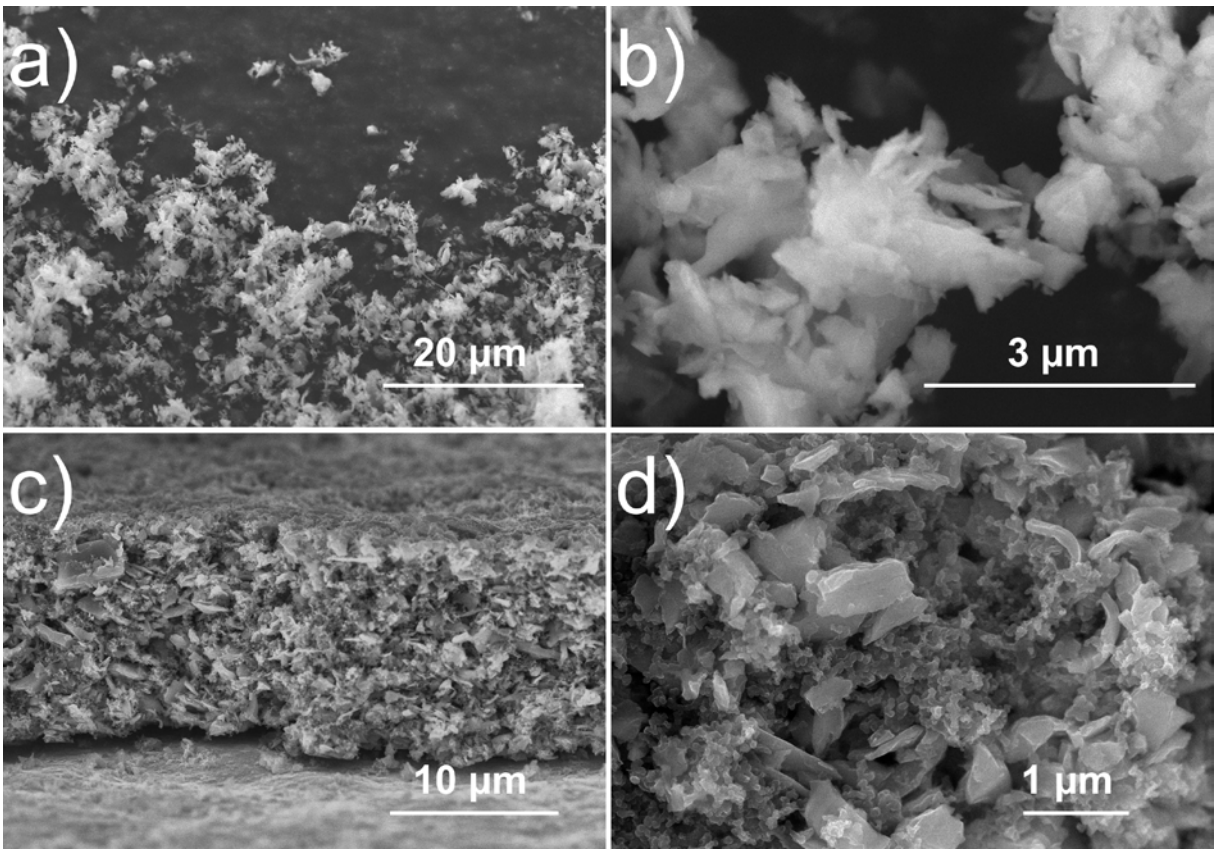

Figure 2. SEM micrographs of diamond wire sawn Si-kerf powder and electrodes of (a) low magnification survey, (b) details of the , (c and d) cross sections of a corresponding electrode at different magnifications.

Cross sectional analysis of a Si-kerf electrode (Figures 2c and 2d, respectively) confirms homogeneous electrode structure with a high degree of porosity. The carbon black particles (spherical particles in the range of 50 nm) can be clearly distinguished from the Si-kerf particles and are homogeneously

distributed in the Si matrix. The electrode thickness was in the range of 10-15 µm. The observed detachment from the Cu current collector is a result of the preparation procedure for SEM imaging.

3.2. Electrochemical characterisation

Electrodes fabricated from both diamond wire cut and blade sawn Si-kerf were assembled into coin cells in a half-cell configuration and galvanostatically cycled. Within this study the effect of the FEC concentration onto the cycling stability was evaluated. FEC is a well-known SEI-aiding additive and decomposes at higher potentials than the other electrolyte components [24]. Under the elimination of the fluorine groups it mainly forms a polymeric matrix with organic and inorganic Li salts such as LiF on the electrode surface [25-27]. A reference sample without the addition of FEC and three different concentrations of FEC, 5, 10 and 15 vol. % were evaluated. As the Si-kerf exhibits a rather high surface area, a considerable level of SEI formation was expected. All half-cells were subject to a slow four-cycle formation process, where the specific capacity was limited to 500, 1000, 1500 and 2000 mAh g^{-1} of Si. Since state-of-the-art cathode materials offer rather low specific capacity values of 140-200 mAh g^{-1}, an anode capacity of 1000-2000 mAh g^{-1} would be sufficient to ensure a high specific energy of the resulting full-cell. Even higher capacities, which are in principle possible with Si as anode material, would result in only minor increases in the overall specific energy and come with the expense of severe volume changes of the anode. Accordingly, it was not the goal of this study to reach lithiation values close to the theoretical maximum and so a rather high cut-off voltage of 50 mV was used. Figure 3a shows the typical voltage profile of Si-kerf half-cells upon the four-cycle formation. The formation curves of all samples are displayed in the supplementary information (Figure S3). The change in the voltage profile upon lithiation is caused by the proceeding amorphisation upon formation of a Li-Si alloy. Figure 3b shows the rate acceptance of the Si-kerf with a 15 vol. % FEC containing electrolyte. After the initial four-cycle formation, the cell was charged and discharged at different C-rates from low rates of C/20 (180 mA g^{-1}) to very high rates of 1C (3600 mA g^{-1}) for 5 cycles each. After the highest rates cycling at 1C, the cell was cycled at C/20 again to determine if the initial capacity could be restored. At low rates the Si-kerf delivers a high capacity of 2500 mAh g^{-1} and even at a relatively high rate of C/2 the capacity of the Si-kerf demonstrates capacity over 1000 mAh g^{-1}. At the highest applied rate of 1C, capacities of 500 to 700 mAh g^{-1} were achieved and when the rate was reduced again, 95% of the initial capacity was

recovered. The good rate acceptance of the electrode is attributed to the good electrical connectivity by the carbon black matrix of the electrode, and to the addition of FEC to the electrolyte. FEC forms a thinner and more stable SEI layer on the surface of the electrode materials, which minimises the overpotential caused by Li ion migration through the SEI [24-25].

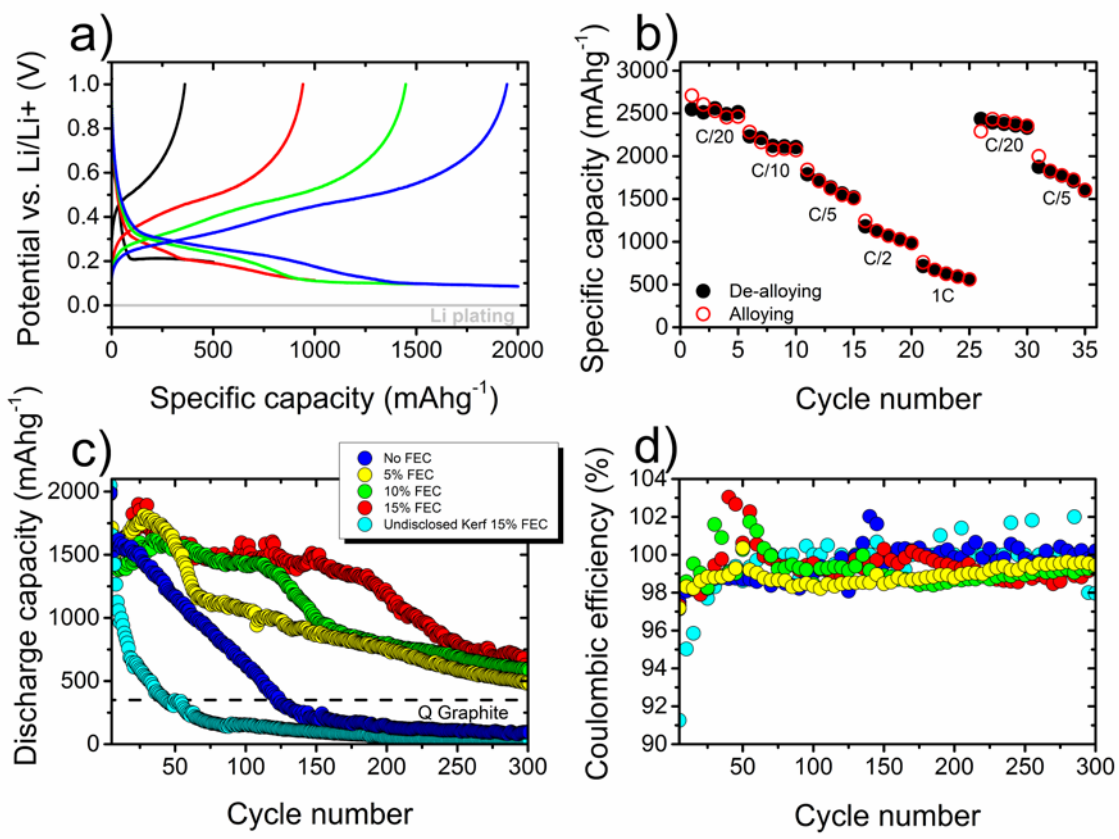

Figure 3. Half-cell cycling of Si-kerf electrodes of (a) Increasing capacity four cycle formation profile of a Si-kerf half-cell (1st cycle black, 2nd cycle red, 3rd cycle green and 4th cycle blue). The Li reduction potential is added as guide for the eye, (b) Rate performance of a Si-kerf half-cell with 15 vol.% FEC in the electrolyte, (c) Alloying capacity at C/5 of Si-kerf half-cells with three different FEC concentrations added to the electrolyte, (d) Coulombic efficiencies of the corresponding samples from Figure 3c.

The long-term cycling results at C/5 of the Si-kerf with different FEC concentrations are given in Figure 3c, with the corresponding coulombic efficiency values in Figure 3d. Charge and discharge voltage profiles displaying the lithiation and delithiation processes in more detail are given in Figure S4, supplementary information. To increase the readability of figure 3d, the coulombic efficiency of every

fifth cycle is plotted. All Si-kerf samples exhibit an initial drop in capacity followed by an increase to values between 1500-2000 mAh g^{-1}. Afterwards, the capacity stabilises and shows only a minor decrease depending on the FEC concentration. At the same time as the capacity increases after the initial drop, the coulombic efficiency reaches values close to 100%. In the case of high FEC concentration the coulombic efficiency exceeds 100% before stabilising. It cannot be concluded if this is due to additional electrolyte reaction, measurement inaccuracy or the mobilisation of prior trapped Li in the samples. The sample containing 5 vol.% FEC started deteriorating after approximately 45 cycles, while the sample containing 10 vol.% FEC began to show a rapid loss in capacity after 122 cycles and the sample containing 15 vol.% FEC after 190 cycles. All FEC containing samples offered capacities higher than the theoretical values of graphite after 300 cycles. The sample without FEC, in contrast, began to deteriorate after 20 cycles and the capacity dropped to values below the theoretical value of graphite after 120 cycles. The direct comparison to other studies using Si-kerf is often difficult as most studies employed extensive post processing, lithiated to lower potentials or simply showed fewer cycles. The results on unprocessed Si-kerf presented in this study are comparable or surpassing studies that post processed their Si-kerf by spray drying, high energy milling, RTP processing, binder pyrolysis and blending with graphene materials [14-17]. Two studies performed by Zhang et al. and Kasukabe et al. showed promising results [19] [13]. In the former study the authors removed the native oxide layer and later on generated an artificial oxide layer. The latter study used extensive bead milling. Wetjen et al. report that the degradation mechanism of a Si-containing electrode can be distinguished into two phenomena which the authors term "silicon particle degradation" and "electrode degradation" [28]. The former is caused by the intrinsic properties of the Si and the latter is dictated by the electrode composition. As all electrodes in this study were processed identically, the difference in degradation is explained by the level of FEC in the electrolyte. The volume changes upon lithiation and delithiation of Si cause the SEI to detach upon delithiation and to be repaired in the following lithiation step. This causes a constant consumption of FEC upon cycling. Jung et al. analysed the consumption of FEC upon cycling of Si containing electrodes and found that the point at which a rapid capacity decay occurs corresponds to the point at which the electrolyte is FEC depleted [29]. Concurrent to this, a steep drop in the coulombic efficiency is observed, as is shown in Figure 3d. This steep capacity decay flattens out for all samples that contained FEC in the electrolyte and is less pronounced in the sample containing 15 vol.% FEC. The blade-sawn Si-kerf did not show any stable cycles and deteriorated rapidly and reached values

lower than the theoretical capacity of graphite already after 50 cycles. Even the addition of 15 vol.% FEC did not stabilise the cycling behaviour. This Si-kerf sample originating from ingot blade sawing has a lower purity with respect to metal contamination, and a substantially larger particle size (Figure S2). The inferior cycling stability reflects the importance of these variables and is most likely governed by the difference in particle size of this Si-kerf. For materials to be used in battery applications then the method of silicon cutting, and in particular its' impact on the final particle size of the kerf, is a critical variable. Following amorphisation of crystalline Si in the first cycles, the lithiation and delithiation of amorphous (a-Si) occurs in different steps, where the first lithiation step resulting in a-$Li_{2+x}Si$ is located at about 0.25V vs. Li/Li^+ and the further lithiation resulting in an a-$Li_{3+x}Si$ structure occurs at approximately 75 mV vs. Li/Li^+. At even lower potentials a crystalline $Li_{15}Si_4$ phase forms [30-31]. As the cut-off voltage in this study was set to 50 mV, the crystallisation of $Li_{15}Si_4$ should not occur. On delithiation, a-$Li_{3+x}Si$ is delithiated to a-$Li_{2+x}Si$ at about 0.3 V vs. Li/Li^+ and a-$Li_{2+x}Si$ is finally delithiated to a-Si at about 0.4-0.5 V vs. Li/Li^+ resulting in differential capacity curves with two peaks on (de)lithiation. Figure 4 shows a 2D representation of the reduced differential capacity (dQ/dV) upon delithiation, plotted as a function of the cycle number, for cells with different amounts of FEC. The complete dQ/dV data used to generate the contour plots are given in the supplementary information (Figure S5, supplementary information). In all cases where FEC was added to the electrolyte the two distinct delithiation peaks are visible after the first few cycles. In the case, where no FEC was added to the electrolyte, the peak corresponding to the delithiation of a-$Li_{3+x}Si$ is much less pronounced and disappears over the first fifty cycles. In all cases the delithiation peak of a-$Li_{3+x}Si$ disappears at the point where the severe capacity fade begins, which is believed to correspond to the point where the electrolyte FEC is depleted and the other electrolyte components begin to be consumed, resulting in extensive SEI growth. Such SEI growth will have a profound effect on the overpotential of (de)lithiation, as it increases the resistance to Li ion transport and increases the internal cell resistance. Consequently, the conversion potential of a-$Li_{2+x}Si$ to a-$Li_{3+x}Si$ is shifted below the cut-off of 50 mV. This is evident from the complete dQ/dV plots shown in the supplementary information (Figure S5). The instability of the SEI and the resulting consumption of FEC and other electrolyte components during cycling is believed to be the major cause of the capacity fade, and a high amount of FEC is required to ensure a high cycle-life of the Si-kerf anodes.

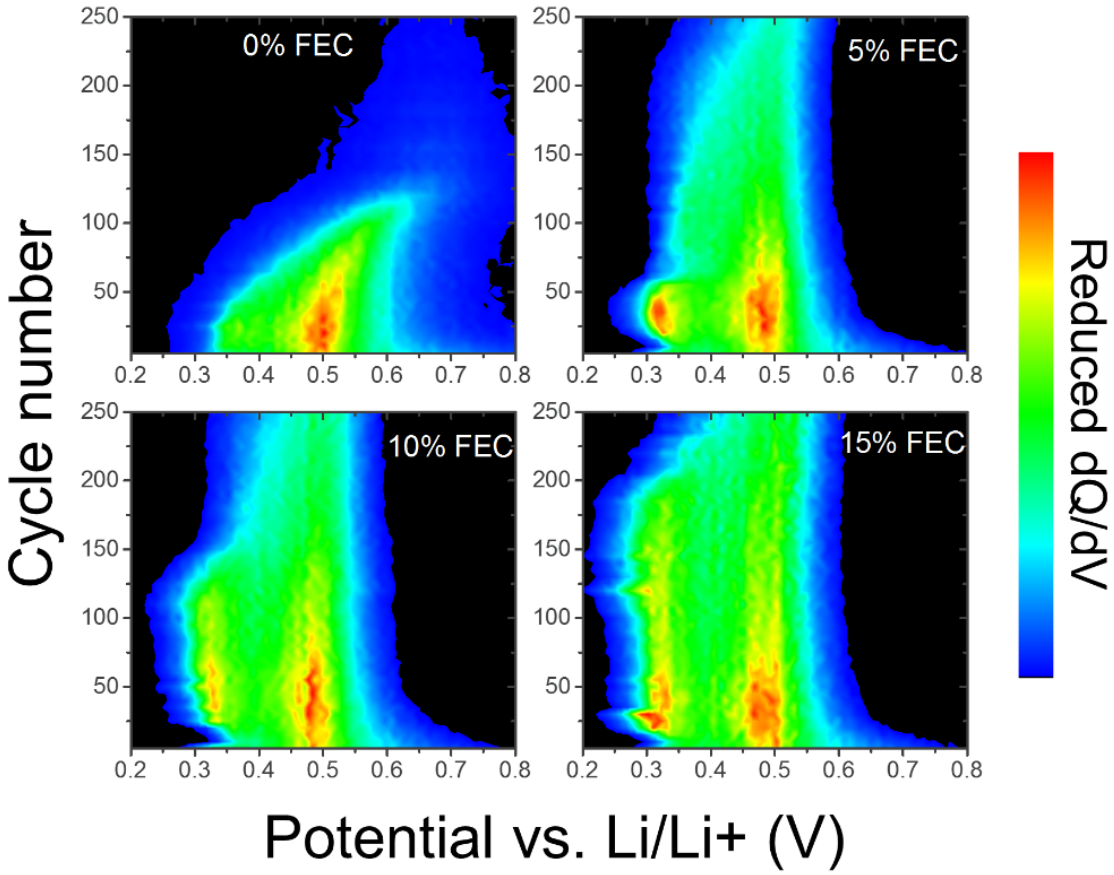

Figure 4. Contour plots of the differential capacity (dQ/dV) upon delithiation over 250 cycles for the sample with 0, 5, 10 and 15 vol.% FEC with a resolution in the y direction of 5 cycles. The colour scales from black (low) to red (high).

For operation as an anode in a LiB, it is of primary importance that the material can deliver a stable capacity over a large number of cycles, and within a stable voltage window. A shift in the anode end potential results in a corresponding shift in the overall cell potential, which is undesirable from a cell monitoring and management perspective. To analyse how many cycles the Si-kerf can deliver a stable capacity, the material was cycled with a lithiation limited capacity of 1000 $mAhg^{-1}$ at a C-Rate of C/5, and the end potential of lithiation was monitored. The results are shown in Figures 5a and b, and in accord with previous studies, the stable cycling regime increased with increasing amounts of FEC additive [32-33]. The end of lithiation potential is shown in figure 5, and it is seen that all cells exhibit an

initial drop from values of 0.2 V to approximately 0.125 V vs. Li/Li^+. For the cell without FEC additive, the end of lithiation potential then decreases steadily, reaching the 50mV low voltage cut-off after 79 cycles. The addition of FEC results, in contrast, in a stable end of lithiation potential at ~100mV. The stability of this plateau in potential is proportional to the concentration of the FEC additive, with a relatively rapid decrease to the 50mV low voltage cut-off occurring at the point where the FEC is fully consumed and additional electrolyte decomposition reactions occur. This is reflected also in the coulombic efficiency (Figure 3). For 5% and 10% FEC additions, the 50mV end potential cut-off was triggered after 119 and 210 cycles, respectively. The cell incorporating 15% FEC addition completed 355 cycles before an end of lithiation potential of 50mV was recorded. It also exhibited a much slower fall in end potential, which would suggest the formation of a more stable SEI than the cells with lower FEC content.

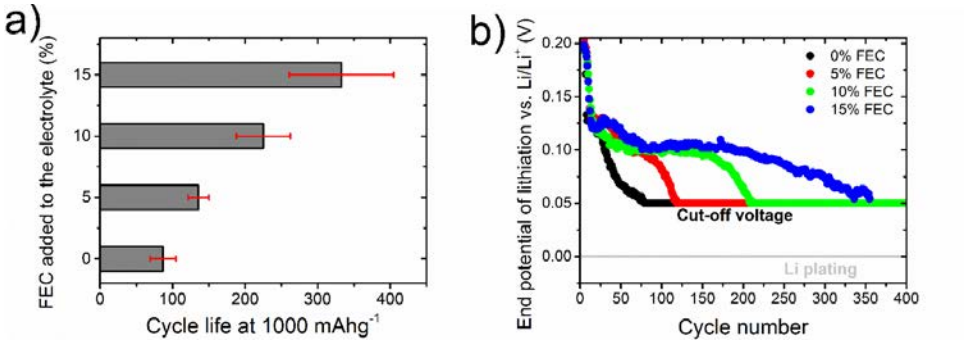

Figure 5. (a) Average cycle life dependency on FEC electrolyte concentration for diamond wire cut Si-kerf half-cells at cycling capacity limit of 1000 mAh g^{-1}. The standard deviations (red error bars) are included. (b) Evolution of the corresponding lithiation end potential.

The recurrent formation of new SEI via FEC consumption also involves the consumption of lithium, and the full impact of this on cell capacity may be masked when testing against a lithium counter electrode, as lithium tends to be present in large excess.

Accordingly, full-cell testing was performed using an NMC 442 cathode vs. the diamond wire cut Si-kerf anode. An FEC additive concentration of 15 vol.% was used, following the observation that this gave

the best results in half-cell configuration. The results are shown in figure 6. For reference the NMC cathode material was tested in half-cell configuration to evaluate its cycling stability for 100 cycles (figure 6a and b). A specific capacity of 150 mAh g^{-1} at a current density of C/10 was recorded, with an initial coulombic efficiency of 84%. The first cycle inefficiency is mainly caused by electrolyte oxidation and the formation of the cathode interface, and by parasitic side reactions on both electrodes. The areal capacity of the cathode was in the range of 1 mAh/cm^2, which then matches to an anode capacity of 800-1000 mAh g^{-1}(Si). The NMC cathode cycled stably with minimal losses at current density of 1C for 100 cycles. The inset of figure 6 b shows the rate acceptance of the cathode delivering good values up to a high rate of 2C.

The voltage profiles of the first two cycles and the corresponding dQ/dV curves of the NMC | Si-kerf Full-cell are shown in figure 6 c and d. The cell was cycled between 2.5 and 4.2 volts and delivered an initial discharge capacity of 148 mAh g^{-1} (NMC) and a first cycle efficiency of 82%. The corresponding anode capacity was approximately 900 mAh g^{-1} (Si) as can be seen in the top abscissa of figure 6 c. The first cycle efficiency is almost as high as the NMC cathode in half-cell arrangement and the NMC | Si full-cell delivered the same capacity during the second discharge. The peak corresponding to the initial SEI formation is located at 2.9V and clearly visible in the dQ/dV plot in figure 6 d. In addition to this electrolyte oxidation and cathode interface formation will contribute to the inefficiency. As described in the previous section, the full-cell was balanced so that the full utilisation of the NMC capacity is equal to about 1000 $mAhg^{-1}$ (Si). This balancing is required to keep the volume changes in the anode limited and to obviate the hazard of Li plating at increased currents. As the Si anode is expected to have an end of lithiation potential of 0.1-0.15 V at this degree of lithiation, the cathode potential will be in the range of 4.3-4.35 V vs. Li/Li^+.

The full-cell was also tested at C-rates of C/10, C2, 1C and 2C upon discharge for 5 cycles each, as shown in Figure 6e. The maximum charge rate was set to C/2 accompanied with a CV step programmed at 4.2V until the current dropped to C/10. The NMC Si-kerf full-cell showed a good rate performance at all evaluated C-rates. When compared to the inset in figure 6b, it appears that the rate performance is dictated by the NMC cathode.

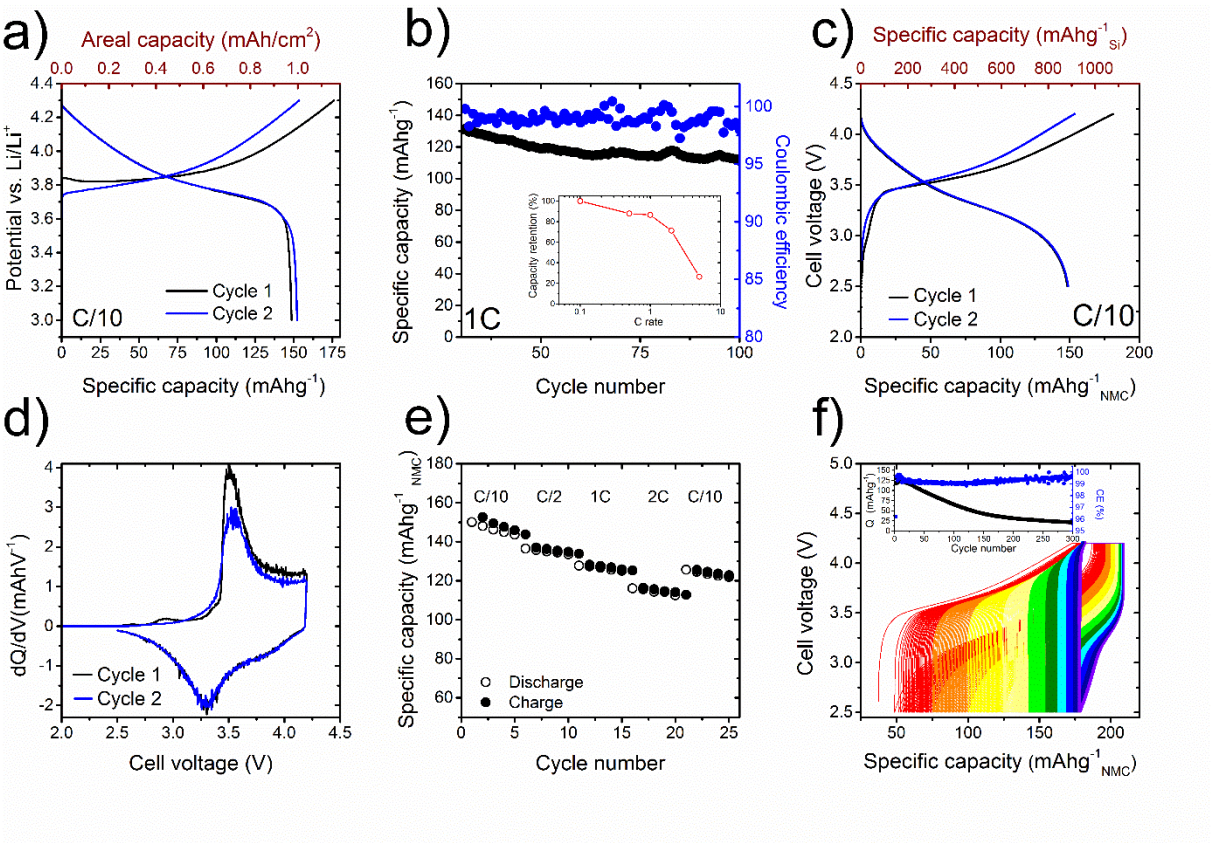

Figure 6. Cycling data of NMC cathodes and NMC/Si full-cells. (a) 3rd cycle of an NMC half-cell at C/10, including specific and areal capacity. (b) Cycle life and rate performance of an NMC half-cell. (c) Formation cycles of an NMC/Si full-cell at C/10. Specific capacity values for both NMC and Si are included. (d) Corresponding differential capacity plots. (e) Rate performance of an NMC/Si Full-cell. (f) Cycle life of an NMC/Si full-cell. Each colour represents 30 cycles. The inset shows an alternative illustration including the coulombic efficiency (CE, %).

To draw a conclusion whether the obtained half-cell results are translatable to a full-cell, the NMC Si-kerf cell was cycled 300 times at a C/2 rate in CC-CV mode upon charge. To draw a conclusion as to whether the obtained half-cell results are translatable to a full-cell, the NMC | Si-kerf cell was cycled 300 times at a C/2 rate in CC-CV mode upon charge. Figure 6f shows the evolution of the voltage profile, where each colour represents 30 cycles. The inset shows the evolution of the specific capacity and the coulombic efficiency. A magnified version of the first 100 cycles of the inset is given in the supplementary information (Figure S6). The cell cycled stably for 15 cycles with a capacity of 120 mAh g^{-1} (NMC), which translates to a capacity of 713 mAh g^{-1} (Si). During the initial 15 cycles the coulombic efficiency was

~99.5% on average. After 15 cycles the coulombic efficiency dropped to 99% and the capacity began to fade, with 80% of the initial value reached after 50 cycles. After about 130 cycles the capacity fade reduced, and the coulombic efficiency values increased to 99.5% again. However, at this point the reversible capacity was ~50 mAh g^{-1} (NMC). The voltage profile revealed a shift in the charging onset potential from ~3.5 V to ~3.85V after 130 cycles. At later stages of cycling this value shifts even higher to values above 4 V and most of the charge is seen to occur during the CV step at 4.2 V. This suggests changes of the state of charge of one or both electrodes upon cycling and is likely to be caused by Li depletion of the cathode. As the voltage profile of a Si electrode is rather sloping in comparison to e.g. graphite, a lower degree of lithiation will cause a higher potential vs. Li/Li^+. This will then cause the end of charge of the cathode to shift to higher potentials vs. Li/Li^+ to sustain a stable potential difference of 4.2 V between both electrodes. The shift towards higher potentials can then shift the cathode outside of the stability limit of the electrolyte. It can also cause further delithiation and destabilisation of the layered cathode structure. This phenomenon was extensively studied and discussed by Beattie et al. using three electrode cells [34]. To confirm that Li depletion of the cathode is the main reason for the strong capacity fade, the full-cell was disassembled after cycling and both electrodes were re-assembled in half-cell configuration. Figure 7 a and b show the corresponding half- cell profiles of the NMC cathode and the Si-kerf anode vs. Li at low currents of C/10 for NMC and C/20 for Si-kerf.

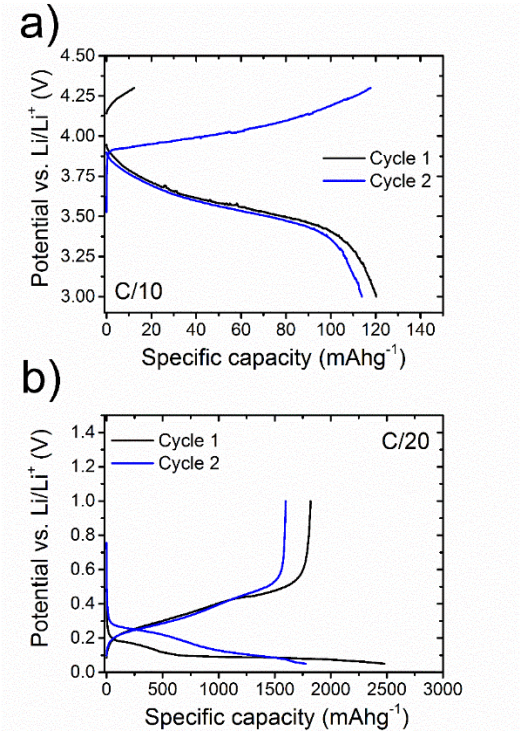

Figure 7. Half-cell profiles of (a) NMC and (b) Si-kerf after 300 cycles in full-cell configuration. The electrodes are the same as presented as full-cell in Figure 6e.

The first charge of the NMC half-cell to a potential of 4.3V vs. Li/Li^+ delivered a low capacity of 12.4 mAh g^{-1}. During the last full-cell cycle the reversible capacity was 21.5 mAh g^{-1} (NMC), but the cathode might have been polarised to higher potentials than 4.3V vs Li/Li^+ during full-cell operation. After the first charge the NMC cathode could be relithiated to values of 120 mAh g^{-1}, where the onset of lithiation was shifted to lower potentials compared to a fresh electrode. The lower capacity and the increased overpotential suggests a degree of electrode degradation, that could have occurred when polarised to high potentials. The Si-kerf anode showed a high first lithiation potential of 2500 mAh g^{-1}, but the during the second cycle the capacity dropped to 1750 mAh g^{-1}. These results verify that the degradation of the full-cell is caused by Li depletion of the cathode. As the Si-kerf anode can be relithiated after 300 cycles, it must be concluded that most active Li is incorporated into the SEI, as both electrodes seem to be depleted. This is expected, as the termination of fluoride upon the reduction of FEC will consume Li, and the half-cells results shown in figure 3, 4 and 5 already suggested that FEC is consumed upon cycling in order to repair the SEI. Hence, the instability of the SEI, which results in the irreversible consumption of Li ions, is the main reason for capacity fade in full-cell configuration.

4. Conclusion

The implementation of recovered Si from diamond wire cutting of Si ingots as anode material for LiBs has been studied. Diamond cutting of Si ingots results in irregular shaped sub-micron Si particles with a high surface area and low levels of metal impurities from the cutting process. The level of metal contamination was measured to be about 110 ppm by ICP-OES and the XRD analysis showed no foreign crystalline phases. In half-cell configuration, the Si-kerf showed stable cycling for up to 200 cycles at a high capacity of 1500 mAh g^{-1} when 15 vol.% FEC were added to the electrolyte as SEI forming additive. When the lithiation capacity was limited to a 1000 mAh g^{-1}, the same sample showed reversible cycling for over 300 cycles. The importance of FEC concentration is clear. Furthermore,

different sawing techniques result in completely different particle size distributions and the Si-kerf from diamond wire cutting was found to be much smaller in size than a commercial processed Si-kerf from blade cutting. The latter showed very poor cycling performance, most likely caused by the difference in particle size, as the purity of the uncleaned diamond wire Si-kerf was comparable to the commercial Si-kerf. Full-cell tests with an NMC 442 cathode were performed to analyse the performance of the recovered Si-kerf in a realistic setup and the failure mechanism. The NMC Si full-cell reached a high capacity of 150 mAh g^{-1} (NMC), while the anode was operating at 900 mAh g^{-1} (Si). The full-cell showed an adequate rate acceptance that appeared to be governed by the cathode, and stable cycling for 15 cycles. After 15 cycles the full suffered from severe capacity fade caused by the irreversible consumption of Li in the SEI, as proven by post-mortem half-cell analysis. It is concluded that pure Si-kerf anodes cannot be satisfactorily stabilised even with high concentrations of FEC.

Acknowledgements

The authors gratefully acknowledge the European commission for funding the Eco Solar project within the European Union's Horizon 2020 research and innovation programme under grant agreement No. 679692. Furthermore, Dr. Edel Sheridan is acknowledged for fruitful discussions, Jannicke Kvello and Dr. Lu Wang are acknowledged for cell assembly and cell testing.

References

1. Tarascon, J. M.; Armand, M., Issues and Challenges Facing Rechargeable Lithium Batteries. *Nature* **2001**, *414*, 359.
2. Nitta, N.; Wu, F.; Lee, J. T.; Yushin, G., Li-Ion Battery Materials: Present and Future. *Materials Today* **2015**, *18*, 252-264.
3. Goodenough, J. B.; Kim, Y., Challenges for Rechargeable Li Batteries†. *Chemistry of Materials* **2010**, *22*, 587-603.
4. Palacin, M. R., Recent Advances in Rechargeable Battery Materials: A Chemist's Perspective. *Chem Soc Rev* **2009**, *38*, 2565-75.
5. Beaulieu, L. Y.; Hatchard, T. D.; Bonakdarpour, A.; Fleischauer, M. D.; Dahn, J. R., Reaction of Li with Alloy Thin Films Studied by in Situ Afm. *Journal of The Electrochemical Society* **2003**, *150*, A1457.

6. Larcher, D.; Beattie, S.; Morcrette, M.; Edström, K.; Jumas, J.-C.; Tarascon, J.-M., Recent Findings and Prospects in the Field of Pure Metals as Negative Electrodes for Li-Ion Batteries. *Journal of Materials Chemistry* **2007**, *17*, 3759.
7. Nitta, N.; Yushin, G., High-Capacity Anode Materials for Lithium-Ion Batteries: Choice of Elements and Structures for Active Particles. *Particle & Particle Systems Characterization* **2014**, *31*, 317-336.
8. Liu, X. H.; Zhong, L.; Huang, S.; Mao, S. X.; Zhu, T.; Huang, J. Y., Size-Dependent Fracture of Silicon Nanoparticles During Lithiation. *ACS Nano* **2012**, *6*, 1522-31.
9. Wang, D.; Gao, M.; Pan, H.; Wang, J.; Liu, Y., High Performance Amorphous-Si@Siox/C Composite Anode Materials for Li-Ion Batteries Derived from Ball-Milling and in Situ Carbonization. *Journal of Power Sources* **2014**, *256*, 190-199.
10. Takamura, T.; Ohara, S.; Uehara, M.; Suzuki, J.; Sekine, K., A Vacuum Deposited Si Film Having a Li Extraction Capacity over 2000 Mah/G with a Long Cycle Life. *Journal of Power Sources* **2004**, *129*, 96-100.
11. Powell, D. M.; Winkler, M. T.; Choi, H. J.; Simmons, C. B.; Needleman, D. B.; Buonassisi, T., Crystalline Silicon Photovoltaics: A Cost Analysis Framework for Determining Technology Pathways to Reach Baseload Electricity Costs. *Energy & Environmental Science* **2012**, *5*, 5874.
12. Tsai, T.-H.; Shih, Y.-P.; Wu, Y.-F., Recycling Silicon Wire-Saw Slurries: Separation of Silicon and Silicon Carbide in a Ramp Settling Tank under an Applied Electrical Field. *Journal of the Air & Waste Management Association* **2013**, *63*, 521-527.
13. Kasukabe, T.; Nishihara, H.; Kimura, K.; Matsumoto, T.; Kobayashi, H.; Okai, M.; Kyotani, T., Beads-Milling of Waste Si Sawdust into High-Performance Nanoflakes for Lithium-Ion Batteries. *Sci Rep* **2017**, *7*, 42734.
14. Kim, S. K.; Kim, H.; Chang, H.; Cho, B. G.; Huang, J. X.; Yoo, H.; Kim, H.; Jang, H. D., One-Step Formation of Silicon-Graphene Composites from Silicon Sludge Waste and Graphene Oxide Via Aerosol Process for Lithium Ion Batteries. *Scientific Reports* **2016**, *6*, 8.
15. Tan, H. G.; Duh, J. G., Processing Silicon Microparticles Recycled from Wafer Waste Via Rapid Thermal Process for Lithium-Ion Battery Anode Materials. *Journal of Power Sources* **2016**, *335*, 146-154.
16. Bao, Q.; Huang, Y. H.; Lan, C. K.; Chen, B. H.; Duh, J. G., Scalable Upcycling Silicon from Waste Slicing Sludge for High-Performance Lithium-Ion Battery Anodes. *Electrochimica Acta* **2015**, *173*, 82-90.
17. Chou, C. Y.; Kuo, J. R.; Yen, S. C., Silicon-Based Composite Negative Electrode Prepared from Recycled Silicon-Slicing Slurries and Lignin/Lignocellulose for Li-Ion Cells. *Acs Sustainable Chemistry & Engineering* **2018**, *6*, 4759-4766.
18. Chen, C.-J.; Mori, T.; Jena, A.; Lin, H.-Y.; Yang, N.-H.; Wu, N.-L.; Chang, H.; Hu, S.-F.; Liu, R.-S., Optimizing the Lithium Phosphorus Oxynitride Protective Layer Thickness on Low-Grade Composite Si-Based Anodes for Lithium-Ion Batteries. *ChemistrySelect* **2018**, *3*, 729-735.
19. Zhang, L.; Zhang, L.; Zhang, J.; Hao, W.; Zheng, H., Robust Polymeric Coating Enables the Stable Operation of Silicon Micro-Plate Anodes Recovered from Photovoltaic Industry Waste for High-Performance Li-Ion Batteries. *Journal of Materials Chemistry A* **2015**, *3*, 15432-15443.
20. Mazouzi, D.; Lestriez, B.; Roué, L.; Guyomard, D., Silicon Composite Electrode with High Capacity and Long Cycle Life. *Electrochemical and Solid-State Letters* **2009**, *12*, A215.
21. Reyter, D.; Rousselot, S.; Mazouzi, D.; Gauthier, M.; Moreau, P.; Lestriez, B.; Guyomard, D.; Roué, L., An Electrochemically Roughened Cu Current Collector for Si-Based Electrode in Li-Ion Batteries. *Journal of Power Sources* **2013**, *239*, 308-314.
22. Philippe, B.; Dedryvere, R.; Gorgoi, M.; Rensmo, H.; Gonbeau, D.; Edstrom, K., Improved Performances of Nanosilicon Electrodes Using the Salt Lifsi: A Photoelectron Spectroscopy Study. *J Am Chem Soc* **2013**, *135*, 9829-42.
23. Raider, S. I.; Flitsch, R.; Palmer, M. J., Oxide Growth on Etched Silicon in Air at Room Temperature. *Journal of The Electrochemical Society* **1975**, *122*, 413-418.

24. Choi, N.-S.; Yew, K. H.; Lee, K. Y.; Sung, M.; Kim, H.; Kim, S.-S., Effect of Fluoroethylene Carbonate Additive on Interfacial Properties of Silicon Thin-Film Electrode. *Journal of Power Sources* **2006**, *161*, 1254-1259.
25. Markevich, E.; Salitra, G.; Aurbach, D., Fluoroethylene Carbonate as an Important Component for the Formation of an Effective Solid Electrolyte Interphase on Anodes and Cathodes for Advanced Li-Ion Batteries. *ACS Energy Letters* **2017**, *2*, 1337-1345.
26. Jaumann, T., et al., Lifetime Vs. Rate Capability: Understanding the Role of Fec and Vc in High-Energy Li-Ion Batteries with Nano-Silicon Anodes. *Energy Storage Materials* **2017**, *6*, 26-35.
27. Michan, A. L.; Parimalam, B. S.; Leskes, M.; Kerber, R. N.; Yoon, T.; Grey, C. P.; Lucht, B. L., Fluoroethylene Carbonate and Vinylene Carbonate Reduction: Understanding Lithium-Ion Battery Electrolyte Additives and Solid Electrolyte Interphase Formation. *Chemistry of Materials* **2016**, *28*, 8149-8159.
28. Wetjen, M.; Pritzl, D.; Jung, R.; Solchenbach, S.; Ghadimi, R.; Gasteiger, H. A., Differentiating the Degradation Phenomena in Silicon-Graphite Electrodes for Lithium-Ion Batteries. *Journal of The Electrochemical Society* **2017**, *164*, A2840-A2852.
29. Jung, R.; Metzger, M.; Haering, D.; Solchenbach, S.; Marino, C.; Tsiouvaras, N.; Stinner, C.; Gasteiger, H. A., Consumption of Fluoroethylene Carbonate (Fec) on Si-C Composite Electrodes for Li-Ion Batteries. *Journal of The Electrochemical Society* **2016**, *163*, A1705-A1716.
30. Key, B.; Morcrette, M.; Tarascon, J. M.; Grey, C. P., Pair Distribution Function Analysis and Solid State Nmr Studies of Silicon Electrodes for Lithium Ion Batteries: Understanding the (De)Lithiation Mechanisms. *J Am Chem Soc* **2011**, *133*, 503-12.
31. Huang, Q.; Loveridge, M. J.; Genieser, R.; Lain, M. J.; Bhagat, R., Electrochemical Evaluation and Phase-Related Impedance Studies on Silicon-Few Layer Graphene (Flg) Composite Electrode Systems. *Sci Rep* **2018**, *8*, 1386.
32. Nakai, H.; Kubota, T.; Kita, A.; Kawashima, A., Investigation of the Solid Electrolyte Interphase Formed by Fluoroethylene Carbonate on Si Electrodes. *Journal of The Electrochemical Society* **2011**, *158*, A798.
33. Lin, Y. M.; Klavetter, K. C.; Abel, P. R.; Davy, N. C.; Snider, J. L.; Heller, A.; Mullins, C. B., High Performance Silicon Nanoparticle Anode in Fluoroethylene Carbonate-Based Electrolyte for Li-Ion Batteries. *Chem Commun (Camb)* **2012**, *48*, 7268-70.
34. Beattie, S. D.; Loveridge, M. J.; Lain, M. J.; Ferrari, S.; Polzin, B. J.; Bhagat, R.; Dashwood, R., Understanding Capacity Fade in Silicon Based Electrodes for Lithium-Ion Batteries Using Three Electrode Cells and Upper Cut-Off Voltage Studies. *Journal of Power Sources* **2016**, *302*, 426-430.